

On collisional free-free photon absorption in warm dense matter

J. Meyer-ter-Vehn¹ and R. Ramis²

¹*Max-Planck-Institut für Quantenoptik, Hans-Kopfermann-Str. 1, Garching 85748, Germany*

²*E.T.S.I. Aeronáutica y del Espacio, Universidad Politécnica de Madrid, P. Cardenal Cisneros 3, Madrid 28040, Spain*

(Dated: 24 July 2019)

The rate of photon absorption in warm dense matter (WDM) induced by free-free electron-ion collisions is derived from Sommerfeld's cross-section for non-relativistic bremsstrahlung emission, making use of detailed balance relations. Warm dense matter is treated as a metal-like state in the approximation of a uniform degenerate electron gas and a uniform ion background. Total absorption rates are averaged over the electron Fermi distribution. A closed expression is obtained for the absorption rate, depending on temperature, density, and photon energy, that scales with ion charge Z . It is evaluated numerically for the full parameter space, which requires different representations of the hypergeometric functions involved. The results are valid for photon frequencies larger than the plasma frequency of the medium. They are compared with approximate formulas in various asymptotic regions.

I. INTRODUCTION

Recent achievements in generating ultra-short high-power photon and particle pulses allow to produce small uniform volumes of warm dense matter (WDM), a metal-like plasma state of high density and temperature in the range of the Fermi temperature. These plasma states play an important role in high-energy density physics related to inertial confinement fusion¹ and novel radiation sources². They are also of fundamental interest, because they fill the gap in the phase diagram between classical high-temperature plasma and solid matter. Photon absorption by target electrons is the basic process when generating WDM with pulses from the x-ray free electron lasers (XFEL), e.g. now available at Stanford³ and DESY⁴. The XFEL beams are used for both generating and probing WDM. Also laser-generated beams of high laser harmonics have been used to probe free-free absorption in solid aluminum⁵; the comb of high harmonics allows to measure absorption at different frequencies in a single shot.

The present paper is devoted to collisional absorption of soft X-rays in WDM, which is the free-free part of the total absorption. Though absorption by bound-free and bound-bound transitions (in case they are admitted) often dominates the total rate, here we restrict ourselves to the contribution of free electrons and consider, in particular, the case of fully ionized plasmas.

The central idea of the present paper is to derive the rate of photon absorption from the cross-section for bremsstrahlung, making use of detailed balance relations. The differential cross-section of bremsstrahlung emitted during Coulomb scattering of electrons by ions was first derived quantum-mechanically by Sommerfeld⁶. It is valid not only in the limit of fast electrons, where $Ze^2/\hbar v \ll 1$ and the Born approximation apply, but also covers slow electrons in the region $Ze^2/\hbar v \approx 1$, which is relevant for WDM and where Coulomb scattering is strongly modified. Here Ze is the ion charge, $\hbar = h/(2\pi)$

Planck's constant, and v the electron velocity. The rate of spontaneous photon absorption is then corrected for stimulated emission and averaged over the Fermi distribution, describing the degenerate electrons in WDM. This provides the coefficient for total free-free photon absorption. It depends on three parameters: temperature and density of electrons as well as photon energy.

The procedure makes use of the Drude-Sommerfeld model; for a modern presentation, see the book of Ashcroft and Mermin on solid state physics⁷. It describes electrons as a Fermi gas of independent particles that collide with ions. The collision frequency ν was used as a parameter and adjusted to experiments. In the present approach, however, we consider inverse bremsstrahlung collisions explicitly to describe photon absorption. The assumption of a uniform Fermi gas is certainly a rough approximation for WDM, in particular when approaching zero temperature and high densities above solid density. For these regions, we cannot expect that the present approach leads to quantitative agreement with experiments. However, it allows us to obtain closed formulas and scaling relations covering a wide region of the parameter space. This is a major objective of the present paper. It may serve as a general reference when using more sophisticated theory. Making use of the quantum-statistical approach to WDM, optical properties have been treated in a number of papers (see e.g. Ref. 8 and papers quoted therein). Recently, density functional theory has been successfully applied to absorption measurements in solid aluminum at low temperatures and frequencies below the L-shell edge, where only valence electrons contribute⁵. Also in order to account for effects at high density, the temperature-dependent Thomas-Fermi model has been used⁹.

In the present paper, we restrict ourselves to frequencies above the plasma frequency, $\omega > \omega_p$, where radiative collisions occur close to the ions at distances $\sim v/\omega$ smaller than the Debye length and collective plasma effects like screening of the Coulomb potential or ion-ion correlations play a minor role. Here v is a typical electron

velocity such as the Fermi velocity, $\omega_p = \sqrt{4\pi e^2 n/m}$ is the plasma frequency, n the electron number density, and m the electron mass. Under the present assumptions, we make use of linear plasma theory. The photon absorption coefficient α is then related to the collision frequency by

$$\alpha = \frac{\nu}{cn_R} \frac{\omega_p^2}{\omega^2}, \quad (1)$$

where $n_R = (1 - \omega_p^2/\omega^2)^{1/2}$ is the index of refraction and c is the velocity of light¹. For dilute high-temperature plasma, the Spitzer collision frequency¹⁰

$$\nu_{\text{Spitzer}} = \frac{4\sqrt{2}\pi}{3} \frac{Zne^4}{\sqrt{m}(kT)^{3/2}} \ln \frac{2\sqrt{3}kT}{\hbar\omega_p} \quad (2)$$

is typically used to describe electron-ion collisions. It diverges for $kT \rightarrow 0$ and does not apply to WDM. The present approach reproduces the Spitzer formula as an upper limit for high temperatures and $\omega \rightarrow \omega_p$. It also naturally describes the transition $kT \rightarrow 0$ without introducing any ad hoc cut-offs. The results will be presented in terms of an effective dynamic collision frequency $\nu_{\text{eff}}(\omega)$. Finite values of ν_{eff} are not only due to Fermi degeneracy, but also due to a smooth transition from 'fast' to 'slow' electron scattering, implicit in the fully quantum-mechanical treatment.

The paper is organized as follows: In Sec. II, the central formula for the effective collision frequency $\nu_{\text{eff}}(\omega)$ in warm dense matter is derived. Sec. III is devoted to the numerical evaluation and a discussion of ν_{eff} . Sec. IV provides formulas for various asymptotic regions. Appendix A describes how the hypergeometric function is evaluated in various parameter regions. In Appendix B approximate formulas are derived for different asymptotic regions. Appendix C deals with numerical integration.

Only in the final stages of preparing this manuscript, we became aware of parallel work in the astrophysical literature, concerned with radiative energy transport in stellar interiors as well as interstellar matter. Following

the pioneering work of Kramers in 1923¹¹ and Gaunt in 1930¹², it has become common practice in astrophysics to describe radiative Coulomb collisions by Kramers's quasi-classical cross-section times a quantum-mechanical correction, the so-called Gaunt factor. As it turns out, Sommerfeld's cross-section, on which the present work is based, can also be represented in this way, thus providing a general expression for the free-free Gaunt factor. Following the seminal paper by Karzas & Latter¹³, recent papers¹⁴⁻¹⁶ have been devoted to an accurate numerical determination of the free-free Gaunt factor. They present results similar to ours. An important difference is that thermal averages are discussed only for Maxwell distributions, adequate for the envisioned astrophysical applications, while the present focus is on degenerate plasmas which requires averages over Fermi distributions. Also we discuss in detail the asymptotic limits. We expect that a careful comparison with the astrophysical work, not yet given here, will lead to fruitful extensions of the present work.

II. DERIVATION OF THE COLLISIONAL PHOTON ABSORPTION RATE

A. The cross-section for bremsstrahlung

We start from Sommerfeld's quantum-mechanical result for the differential cross-section of spontaneous bremsstrahlung emission⁶. It describes the scattering of a non-relativistic electron with momentum p on an ion with charge Ze under emission of a photon with frequency ω , averaged over emission angles and polarizations of the photon. In the main part of this paper, we shall use the notation $p_{\pm} = \sqrt{p^2 \pm 2m\hbar\omega}$ for the momentum of the scattered electron, depending on whether the photon is absorbed or emitted. This notation is also used for the variables $\eta = Z\alpha_f mc/p$ and $\eta_{\pm} = Z\alpha_f mc/p_{\pm}$, characterizing Coulomb wave functions. With the fine-structure constant $\alpha_f = e^2/\hbar c$ and Bohr's radius $a_B = \hbar^2/(me^2)$ the cross-section is given by

$$\frac{d\sigma}{d\omega}(p \rightarrow p_-, \omega) = \frac{64\pi^2}{3} \frac{Z^2 \alpha_f^5 a_B^2}{\omega} \left(\frac{mc}{p}\right)^2 \cdot \frac{\xi}{4} \frac{d|F(i\eta_-, i\eta; 1; \xi)|^2/d\xi}{(1 - e^{-2\pi\eta})(e^{2\pi\eta} - 1)}, \quad (3)$$

here $F(i\eta_-, i\eta; 1; \xi)$ denotes the complete hypergeometric function and $\xi = -4\eta\eta_-/(\eta - \eta_-)^2$.

In passing, we mention already here that Eq. (3) reduces to Kramers's cross-section¹¹

$$\left(\frac{d\sigma(p \rightarrow p_-, \omega)}{d\omega}\right)_{\text{Kram}} = \frac{16\pi}{3\sqrt{3}} \frac{Z^2 \alpha_f^5 a_B^2}{\omega} \left(\frac{mc}{p}\right)^2 \quad (4)$$

in quasi-classical approximation, i.e. for small electron momenta such that $\eta \gg 1$ and $(\eta_- - \eta) \gg 1$. Small

electron momenta in the range of the Fermi momentum play a dominant role in WDM; asymptotic approximations of Eq. (3) will be discussed in detail further below. We notice that Eq. (3) can be written as

$$\frac{d\sigma}{d\omega}(p \rightarrow p_-, \omega) = \left(\frac{d\sigma(p \rightarrow p_-, \omega)}{d\omega}\right)_{\text{Kram}} g_{\text{ff}}, \quad (5)$$

where

$$g_{\text{ff}} = 4\pi\sqrt{3} \cdot \frac{\xi}{4} \frac{d|F(i\eta_-, i\eta; 1; \xi)|^2/d\xi}{(1 - e^{-2\pi\eta_-})(e^{2\pi\eta} - 1)} \quad (6)$$

is the so-called free-free Gaunt factor, used in the astrophysical literature to describe quantum-mechanical corrections to Kramers's quasi-classical cross-section.

B. Detailed balance between photon absorption and photon emission

The central point of this paper is now to derive the rate of collisional photon absorption $R_{\text{abs}}(p, \omega \rightarrow p_+)$; it gives the number of photons with energy $\hbar\omega$ absorbed per unit of time by an electron with momentum p that is boosted to momentum $p_+ = \sqrt{p^2 + 2m\hbar\omega}$, while scattering on an ion with charge Ze . This process is inverse to bremsstrahlung emission and is therefore also called absorption by *inverse* bremsstrahlung. The corresponding rate of bremsstrahlung emission can be calculated from Sommerfeld's cross-section; it is given by

$$R_{\text{em}}(p_+ \rightarrow p, \omega) = \frac{p_+}{m} n_i \frac{d\sigma(p_+ \rightarrow p, \omega)}{d\omega} \Delta\omega \quad (7)$$

and determines the number of photons with frequency between ω and $\omega + \Delta\omega$ emitted per unit of time when an electron with momentum p_+ passes matter having ion density n_i .

The rates for absorption and emission are related by the principle of detailed balance, which is discussed in many textbooks on statistical mechanics (see e.g. Ref. 17). It was used by Einstein in the context of optical transitions to discover stimulated emission¹⁸, the cornerstone of laser physics. Detailed balance relations are derived for systems in statistical equilibrium, but they are valid under much more general conditions. On a microscopic level, detailed balance is related to time reversal symmetry. A brief discussion for practical use is given in Ref. 1. For the ratio of the rates for absorption and emission, one obtains

$$\frac{R_{\text{abs}}(p, \omega \rightarrow p_+)}{R_{\text{em}}(p_+ \rightarrow p, \omega)} = \frac{dZ(\varepsilon_+)/d\varepsilon_+}{dZ(\varepsilon)/d\varepsilon \cdot Z_{\text{ph}}}; \quad (8)$$

it depends only on the number of quantum states available for an electron and/or a photon in the final states of the two processes. For an electron of energy $\varepsilon = p^2/2m$ (and $\varepsilon_+ = p_+^2/2m$, respectively), one finds

$$dZ(\varepsilon)/d\varepsilon = (2/h^3)V_e 4\pi p^2 dp/d\varepsilon = (8\pi m V_e/h^3)p, \quad (9)$$

where $2/h^3$ is the density of quantum states available in phase space for electrons with 2 spin directions and $V_e = 1/n$ is the volume available for one electron. The number of quantum states Z_{ph} available for a photon in the final state, having a frequency between ω and $\omega + \Delta\omega$, is

$$Z_{\text{ph}} = (2/h^3)V_{\text{ph}} 4\pi(\hbar\omega/c)^2(\hbar\Delta\omega/c) = (\omega^2\Delta\omega)/(\pi^2c^3)V_{\text{ph}}, \quad (10)$$

where the photon volume $V_{\text{ph}} = ((E_0^2/8\pi)/\hbar\omega)^{-1}$ is the inverse of the photon number density and E_0 is the amplitude of the electric field of the light wave. Actually, Z_{ph} is the inverse of the photon number per quantum state

$$n_{\text{ph}} = \frac{1}{Z_{\text{ph}}} = \frac{\pi^2c^3}{\omega^2\Delta\omega} \cdot \frac{E_0^2/8\pi}{\hbar\omega}, \quad (11)$$

a quantity needed in the following to describe stimulated emission. From Eqs. (8 - 11) we obtain the important result

$$R_{\text{abs}}(p, \omega \rightarrow p_+) = \frac{p_+}{p} n_{\text{ph}} R_{\text{em}}(p_+ \rightarrow p, \omega). \quad (12)$$

C. The photon absorption density in WDM

We now turn to warm dense matter and show how to apply the relations derived above to a dense degenerate electron gas. First the absorption rate has to be averaged over the Fermi distribution function for the electrons

$$f(p) = \frac{1}{1 + \exp((p^2/2m - \mu)/kT)}, \quad (13)$$

where kT is the electron temperature and the chemical potential μ is determined implicitly by electron density

$$n = \int_0^\infty (2/h^3) 4\pi p^2 dp f(p). \quad (14)$$

The integrated absorption rate per volume then is

$$A_{\text{abs}} = \int_0^\infty \frac{2}{h^3} R_{\text{abs}}(p, \omega \rightarrow p_+) f(p) (1 - f(p_+)) 4\pi p^2 dp; \quad (15)$$

here we account for the case that the final electron state with momentum p_+ is partly occupied in the Fermi gas. Let us also account for stimulated emission of photons with frequency ω , which lowers the electron momentum from p to $p_- = \sqrt{p^2 - 2m_e\hbar\omega}$; it occurs at a rate

$$R_{\text{em}}^{\text{stim}}(p \rightarrow p_-, \omega) = n_{\text{ph}} R_{\text{em}}(p \rightarrow p_-, \omega). \quad (16)$$

This stimulated emission reduces overall absorption. The total absorption rate per volume is therefore obtained as

$$A_{\text{abs}}^{\text{tot}} = \int_0^\infty \frac{2}{h^3} R_{\text{abs}}(p, \omega \rightarrow p_+) f(p) (1 - f(p_+)) 4\pi p^2 dp - \int_{p_{\text{min}}}^\infty \frac{2}{h^3} R_{\text{em}}^{\text{stim}}(p \rightarrow p_-, \omega) f(p) (1 - f(p_-)) 4\pi p^2 dp \quad (17)$$

with $p_{\text{min}} = \sqrt{2m\hbar\omega}$. Now making use of Eq. (12) and Eq. (16) and changing integration variables appropriately, we can combine the two integrals and find

$$A_{\text{abs}}^{\text{tot}} = \frac{8\pi}{h^3} n_{\text{ph}} \int_0^\infty p_+ R_{\text{em}}(p_+ \rightarrow p, \omega) (f(p) - f(p_+)) p dp. \quad (18)$$

D. The effective collision frequency for warm dense matter

Finally, we relate $A_{\text{abs}}^{\text{tot}}$ to the photon absorption coefficient α introduced in Eq. (1) and to an effective dynamic collision frequency $\nu_{\text{eff}}(\omega)$. For this, we notice that $A_{\text{abs}}^{\text{tot}}$ can be expressed also as

$$A_{\text{abs}}^{\text{tot}} = \Phi_{\text{ph}}\alpha = \Phi_{\text{ph}}\left(\frac{\nu_{\text{eff}}}{cn_R}\right)\frac{\omega_p^2}{\omega^2}, \quad (19)$$

where $\Phi_{\text{ph}} = (E_0^2/(8\pi\hbar\omega))cn_R$ denotes the flux of photons, which is given by the photon density $E_0^2/(8\pi\hbar\omega)$ times the group velocity cn_R of the light pulse close to the scattering ion. This allows us to define the effective collision frequency

$$\nu_{\text{eff}}(\omega) = \frac{\omega^2}{\omega_p^2} \frac{\hbar\omega}{E_0^2/8\pi} A_{\text{abs}}^{\text{tot}}. \quad (20)$$

As it turns out, $\nu_{\text{eff}}(\omega)$ is a convenient quantity to express the results of this paper. Making use of Eqs. (7), (11), and (18), we are led to the central result of the present paper:

$$\nu_{\text{eff}}(\omega) = \frac{n_i c^3}{\hbar^3 \omega_p^2 m} \int_0^\infty p_+^2 \frac{d\sigma(p_+ \rightarrow p, \omega)}{d\omega} (f(p) - f(p_+)) p dp \quad (21)$$

This closed expression allows us to calculate the effective dynamic collision frequency for photon absorption in warm dense matter from the cross-section for

bremsstrahlung given in Eq. (3). By means of Eq. (1), it provides also the collisional absorption coefficient α and the free-free opacity $\kappa = \alpha/\rho$, where ρ is the mass density of the absorbing medium.

For further discussion, let us rewrite the cross-section Eq. (3)

$$\frac{d\sigma}{d\omega}(p_+ \rightarrow p, \omega) = \frac{64\pi^2}{3} \frac{Z^2 \alpha_f^5 a_B^2}{\omega} \left(\frac{mc}{p_+}\right)^2 \cdot G(\hat{\varepsilon}, \hat{\omega}), \quad (22)$$

in terms of the dimensionless function

$$G(\hat{\varepsilon}, \hat{\omega}) = \frac{\xi}{4} \frac{d|F(i\eta, i\eta_+; 1; \xi)|^2/d\xi}{(1 - e^{-2\pi\eta})(e^{2\pi\eta_+} - 1)}, \quad (23)$$

where the coordinates are related to each other by

$$\hat{\varepsilon} = \frac{\varepsilon}{Z^2 E_a} = \frac{p^2}{2mZ^2 E_a} = \frac{1}{2\eta^2}, \quad (24)$$

$$\hat{\omega} = \frac{\hbar\omega}{Z^2 E_a}, \quad (25)$$

$$\hat{\varepsilon} + \hat{\omega} = \frac{\varepsilon + \hbar\omega}{Z^2 E_a} = \frac{p_+^2}{2mZ^2 E_a} = \frac{1}{2\eta_+^2}. \quad (26)$$

In terms of function $G(\hat{\varepsilon}, \hat{\omega})$, the effective collision frequency can be written in particularly transparent form:

$$\nu_{\text{eff}}(\omega) = \frac{16\pi}{3} Z\nu_0 \int_0^\infty G\left(\frac{\varepsilon}{Z^2 E_a}, \frac{\hbar\omega}{Z^2 E_a}\right) \left[f\left(\frac{\varepsilon - \mu}{kT}\right) - f\left(\frac{\varepsilon + \hbar\omega - \mu}{kT}\right) \right] \frac{d\varepsilon}{\hbar\omega}, \quad (27)$$

showing explicitly the dependence on ion charge Z , temperature kT , and chemical potential μ , which is related implicitly to the electron density n . Here the Fermi function is given by $f(x) = 1/(1 + e^x)$, $\nu_0 = E_a/\hbar = 4.14 \times 10^{16} \text{ s}^{-1}$ is the atomic frequency unit, and $E_a = \alpha_f^2 mc^2 = me^4/\hbar^2 = 27.2 \text{ eV}$ the atomic energy unit. The key quantity is the kernel function $G(\hat{\varepsilon}, \hat{\omega})$, depending on electron energy and photon energy, both normalized to $Z^2 E_a$. The kernel $G(\hat{\varepsilon}, \hat{\omega})$ describes radiative Coulomb collisions in the full non-relativistic region. It is equivalent to the Gaunt factor defined in Eq. (6).

III. NUMERICAL EVALUATION

The numerical evaluation of Eq. (27) is not straightforward. This is because $G(\hat{\varepsilon}, \hat{\omega})$ involves the hypergeometric function. We develop the required representations for the different parameter regions in Appendix A, based on the Handbook for Mathematical Functions^{19,20}. Asymp-

otic approximations are found in Refs. 6, 21–23, and corresponding expressions are derived in Appendix B.

A. The kernel $G(\hat{\varepsilon}, \hat{\omega})$.

Results of the numerical evaluation of $G(\hat{\varepsilon}, \hat{\omega})$ are depicted in Fig. 1. One observes that the solution curves become straight equidistant lines in the corner regions of Fig. 1. These regions correspond to approximate asymptotic formulas of logarithmic type in the upper tableau (linear-logarithmic scales for $G > 0.1$) and of power-law type in the lower tableau (log-log scales for $G < 0.1$). There are 5 distinct regions, indicated by Roman numbers in Fig. 1. Their location in the $\hat{\varepsilon}, \hat{\omega}$ plane is shown in Fig. 2. The corresponding asymptotic expressions are given in Table 1; they will be derived in Appendix B.

The approximate expression, most relevant in the context of this paper, is found for $(\hat{\varepsilon} + \hat{\omega}) \gg 1$, be it for

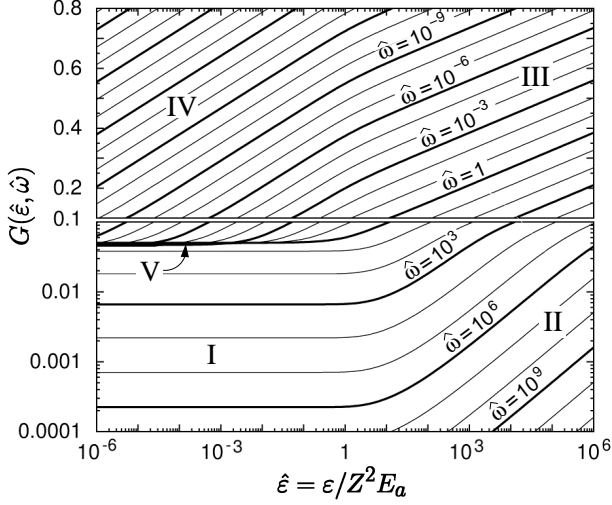


FIG. 1. Function $G(\hat{\varepsilon}, \hat{\omega})$ plotted versus $\hat{\varepsilon}$ for fixed values of $\hat{\omega}$, given as labels in steps of factor 10. Notice that the ordinate scale is logarithmic for $G \leq 0.1$ and linear for $G \geq 0.1$. The Roman numerals identify parameter regions in which $G(\hat{\varepsilon}, \hat{\omega})$ allows for simple asymptotic formulas.

TABLE I. Asymptotic expressions of $G(\hat{\varepsilon}, \hat{\omega})$ for the five regions marked in Fig. 1; $\gamma = 0.577$ is the Euler number.

I	$\hat{\varepsilon} \ll 1, \hat{\omega} \gg 1$	$G(\hat{\varepsilon}, \hat{\omega}) = \frac{1}{\pi\sqrt{2\hat{\omega}}}$
II	$\hat{\varepsilon} \gg 1, \hat{\omega} \gg \hat{\varepsilon}$	$G(\hat{\varepsilon}, \hat{\omega}) = \frac{1}{2\pi^2} \sqrt{\frac{\hat{\varepsilon}}{\hat{\omega}}}$
III	$\hat{\varepsilon} \gg 1, \hat{\omega} \ll \hat{\varepsilon}$	$G(\hat{\varepsilon}, \hat{\omega}) = \frac{1}{4\pi^2} \ln \frac{4\hat{\varepsilon}}{\hat{\omega}}$
IV	$\hat{\varepsilon} \ll 1, \hat{\omega} \ll \hat{\varepsilon}^{3/2}$	$G(\hat{\varepsilon}, \hat{\omega}) = \frac{1}{4\pi^2} \left(\ln \frac{4\sqrt{2}\hat{\varepsilon}^{3/2}}{\hat{\omega}} - \gamma \right)$
V	$\hat{\varepsilon}^{3/2} \ll \hat{\omega} \ll 1$	$G(\hat{\varepsilon}, \hat{\omega}) = \frac{1}{4\pi\sqrt{3}}$

$\hat{\varepsilon} \gg 1$ or $\hat{\omega} \gg 1$ or both:

$$G(\hat{\varepsilon}, \hat{\omega}) \simeq \frac{1}{2\pi} \frac{1/\sqrt{2\hat{\varepsilon}}}{1 - e^{-2\pi/\sqrt{2\hat{\varepsilon}}}} \ln \frac{\sqrt{\hat{\varepsilon} + \hat{\omega}} + \sqrt{\hat{\varepsilon}}}{\sqrt{\hat{\varepsilon} + \hat{\omega}} - \sqrt{\hat{\varepsilon}}}; \quad (28)$$

it reduces to the three sublimits for cases I, II, and III in the appropriate regions. Cases IV and V satisfy $(\hat{\varepsilon} + \hat{\omega}) \ll 1$ and refer to the quasi-classical region: case IV leads to Bohr's classical Coulomb logarithm, and case V reproduces Kramers's classical cross-section for bremsstrahlung (see Eq. (4)). Actually, the whole region V in Fig. 2 maps into essentially a horizontal line at $G \approx 1/(4\pi\sqrt{3})$ in Fig. 1. The Gaunt factor defined by Eq. (6) becomes $g_{\text{ff}} = 1$ for case V.

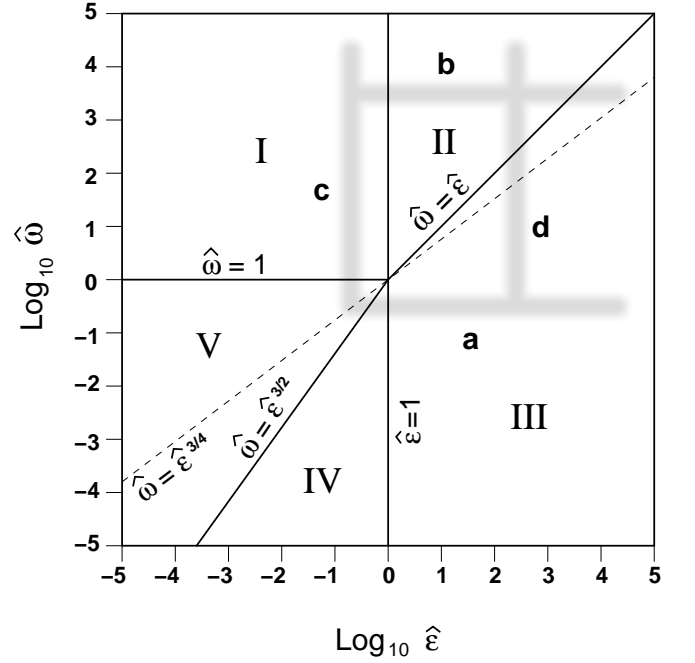


FIG. 2. The $\hat{\varepsilon}, \hat{\omega}$ plane. Roman numerals from I to V mark the five regions, in which asymptotic limits exist. Black solid lines refer to the borders between these regions. The gray-scale lines roughly indicate the parameter region along which asymptotic formulas are compared with exact results in Fig. 3 (horizontal lines a and b) and in Fig. 4 (vertical lines c and b). The broken line ($\hat{\omega} = \hat{\varepsilon}^{3/4}$) locates the lower boundaries $\hat{\omega}_p$ and $\hat{\varepsilon}_F$ for different densities; see text for more explanation.

For intermediate values, close to $\hat{\varepsilon} = 1$ and $\hat{\omega} = 1$ and relevant for WDM and soft X-ray photons, the asymptotic regions connect smoothly. These transitional regions require full numerical evaluation. Notice that, within the present approach, no ad hoc assumptions about cutting off the logarithmic expressions at certain values of their arguments are needed. The effective collision frequencies are obtained by folding $G(\hat{\varepsilon}, \hat{\omega})$ with the Fermi distributions according to Eq. (27). Different regions of $G(\hat{\varepsilon}, \hat{\omega})$ are probed when varying temperature, density, and photon energy. The regions actually probed are bounded from below by the conditions $\omega \geq \omega_p$ and $\varepsilon \geq \varepsilon_F$ and from above by $\hbar\omega \leq mc^2$ and $\varepsilon \leq mc^2$. Here $\varepsilon_F = (\hbar^2/2m)(3\pi^2n)^{2/3}$ is the Fermi energy. Both lower bounds, ω_p and ε_F , depend on density only; in Fig. 2 they are located close to the broken line defined by $\hat{\omega} = \hat{\varepsilon}^{3/4}$.

B. Temperature and frequency dependence of ν_{eff} .

We have chosen hydrogen ($Z = 1$) at solid density ($\rho_0 = 0.086 \text{ g/cm}^3$, $n_0 = 5.14 \times 10^{22} \text{ cm}^{-3}$) as a reference material. At this density, one has $\hbar\omega_p = 8.42 \text{ eV}$ and $\varepsilon_F = kT_F = 5.04 \text{ eV}$. The effective collision frequency ν_{eff} has been calculated numerically according

to Eq. (27) and is plotted in Figs. 3 and 4. In order to illustrate how the limiting analytic approximations agree with these exact numerical solutions, we also show them as broken lines for selected parameters and have labelled them with the Roman letters of the corresponding asymptotic regime. For the comparison, we have chosen the curves for 10 eV and 10 keV photons in Fig. 3, which probe $G(\hat{\varepsilon}, \hat{\omega})$ along the horizontal lines a and b in Fig. 2, and in Fig. 4 the 1 eV and 10 keV isotherms, probing $G(\hat{\varepsilon}, \hat{\omega})$ along the vertical lines c and d, respectively. These lines just provide some guiding for the path through the $\hat{\varepsilon}, \hat{\omega}$ plane, because ν_{eff} actually represents an integral over ε , and we have chosen $\varepsilon \approx kT$ as an average value for this purpose.

In Fig. 3 the collision frequency is plotted as function of temperature for different photon energies. The most prominent feature is that Spitzer's formula Eq. (2) provides the upper limit to ν_{eff} for sufficiently high temperatures ($kT > 10$ eV). Spitzer's result nearly coincides with the curve for 10 eV photons that is close to the plasmon energy $\hbar\omega_p = 8.4$ eV. In Fig. 2 it corresponds to line a in region III. For low temperatures with electron energies $\hat{\varepsilon} < 1$, the Spitzer formula is not valid any more. Here the curve for 10 eV photons saturates at a level of $\nu_{\text{eff}} \approx 2 \times 10^{16} \text{ s}^{-1}$, as described by Eq. (53) obtained for region V. One may notice that line a, before stretching out to region V, also marginally touches region IV. For higher photon energies $\hbar\omega > 10$ eV, ν_{eff} quickly drops. At 100 keV photon energy ($\hat{\omega} \approx 4 \times 10^3$), asymptotic regions I, II, and III (compare line b in Fig. 2) are involved, and formulas Eq. (44), Eq. (46), and Eq. (47) are seen to agree with the exact results in the corresponding regions.

In Fig. 4, the collision frequency is given in terms of isotherms for different photon energies. Here the conspicuous feature is the strip of straight-line isotherms in the temperature range $0 \leq kT \leq \hbar\omega$, scaling with frequency $\propto \omega^{-3/2}$. This behaviour is characteristic for regions I and II and changes rapidly when crossing into region III at higher temperatures (compare Fig. 2). The $\omega^{-3/2}$ scaling leads to the free-free opacity scaling $\kappa = \nu_{\text{eff}}(\omega_p/\omega)^2/(\rho c) \propto \omega^{-7/2}$. It is used in astrophysics (see e.g. Chandrasekhar²⁴) since the pioneering work of Gaunt in 1930¹². The present analysis reveals additional structure, unexplored experimentally so far. More details on the density scaling are given in the next subsection.

C. Density dependence of $\nu_{\text{eff}}(\omega)$

The effective collision frequency derived from Eq. (27) depends on plasma density in a nonlinear way. This is due to the Fermi temperature which scales with density like $kT_F = \varepsilon_F \propto n^{2/3}$. This is illustrated in Fig. 5 together with the density dependence of $\omega_p \propto n^{1/2}$ and the atomic energy unit E_a . The three straight lines cut each other at a density of almost 10^{24} cm^{-3} , independently of Z . This is a factor 20 larger than the electron density n_0

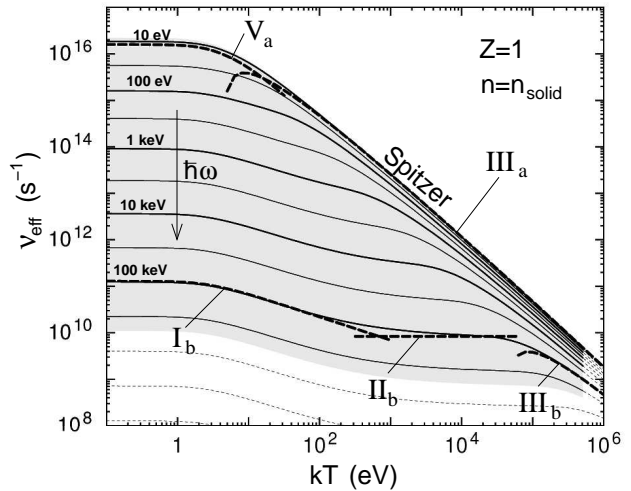


FIG. 3. The dynamic collision frequency for hydrogen ($Z = 1$) at solid density (n_0), given as function of temperature kT for fixed photon energy $\hbar\omega$, both in units of eV. Thick solid lines differ by factors 10. For sufficiently high temperature and small $\hbar\omega$, the curves approach the Spitzer limit, given by Eq. (2). It is almost identical with the $\hbar\omega = 10$ eV curve and is close to the plasma frequency $\hbar\omega_p = 8.3$ eV, which represents the lower frequency bound. Actually, the broken lines give the asymptotic formulas along the horizontal lines shown in Fig. 2. Line a for $\hbar\omega = 10$ eV touches regions III and V (marginally region IV in between), and line b for $\hbar\omega = 100$ keV touches regions I, II, and III. One observes that the asymptotic formulas agree with the exact calculations in the limited temperature regions, given in Sec. IV. All curves are cut off at $kT = mc^2 = 511$ keV, which is the limit for the non-relativistic theory.

of solid hydrogen. The three quantities are related by

$$\frac{\hat{\omega}_p^2 Z}{\hat{T}_F^{3/2}} = \frac{(\hbar\omega_p)^2}{(k_B T_F)^{3/2} (E_a)^{1/2}} = \frac{8\sqrt{2}}{3\pi}. \quad (29)$$

Laser plasmas generated by optical light are an example for densities typically below 10^{21} cm^{-3} , where $kT_F \ll \hbar\omega_p \ll E_a$ and Fermi degeneracy plays no role. On the other hand, applications to inertial confinement fusion require highly compressed hydrogen fuel with densities up to 10^{26} cm^{-3} , and one has $E_a \ll \hbar\omega_p \ll kT_F$. Here the electrons at the Fermi edge have energies of 1 keV, and photons of 0.5 - 1 keV energy propagate in degenerate plasma. This implies that mainly regions II and III in the right half of Fig. 1 contribute to the integral Eq. (27). Densities occurring in the interior of the sun are also depicted in Fig. 5, for comparison; they extend over the whole density range and are located well above kT_F in the non-degenerate regime.

Full numerical results for a large range of densities are shown in Fig. 6. The cut-off energy $\hbar\omega_p$ for photon propagation (shown by arrows) shifts to the right with increasing density. The strip of isotherms showing $\omega^{-3/2}$ scaling

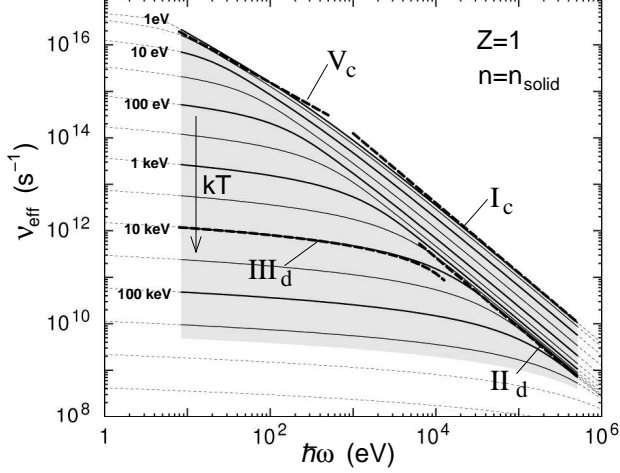


FIG. 4. The dynamic collision frequency for photon absorption in hydrogen ($Z = 1$) at solid density (n_0), now plotted versus photon energy $\hbar\omega$ at fixed temperatures kT . The results are shown as solid curves in the range of validity $\hbar\omega_p < \hbar\omega < mc^2$ and $kT < mc^2$. Consecutive curves differ in temperature by a factor $\sqrt{10}$. The broken lines refer to the approximate formulas derived in Sec. V. A strip of straight isotherms extends between $0 \leq kT \leq \hbar\omega$. It scales $\propto \omega^{-3/2}$ for high photon energies $\hbar\omega \gg kT$. The scaling becomes closer to $\nu_{\text{eff}} \propto \omega^{-1}$ for small temperatures and photon energies comparable to E_a . Again Roman numerals refer to asymptotic regions specified in Fig.2 by vertical lines; line c corresponds to $kT = 1\text{eV}$ and runs through regions I and V, while line d is for $kT = 10\text{keV}$ and extends into regions II and III.

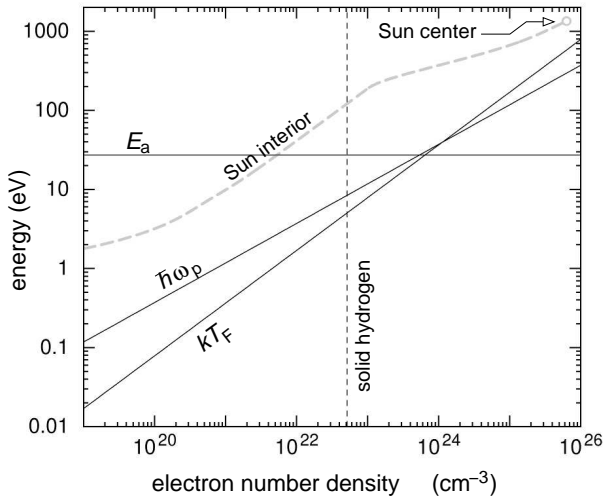


FIG. 5. Fermi energy kT_F , plasmon energy $\hbar\omega_p$, and atomic energy unit E_A plotted as function of electron number density n . The dashed line marks the density n_0 of solid hydrogen. For comparison, also the temperature inside the sun is given versus density²⁵.

decreases in width for increasing n . This is because the lower boundary scales like $\nu_{\text{eff}} \propto (T_F/\omega)^{3/2} \propto n$, while the upper bound obeys $\nu_{\text{eff}} \propto T_F/\omega^{3/2} \propto n^{2/3}$ (compare Eqs.(45) and (46) in Sec. IV). One may also notice that, for the low-temperature isotherms, the transition from $\omega^{-3/2}$ to quasi-classical ω^{-1} scaling is clearly visible only for very low densities. At very high densities, a kink is seen in the uppermost isotherms corresponding to degenerate plasma ($kT \ll kT_F$). This kink appears when $\hbar\omega$ falls below kT_F ; then only a fraction of target electrons with energies $\varepsilon > kT_F - \hbar\omega$ can contribute to photon absorption.

Let us finally discuss the upper limit of ν_{eff} in Fig. 6. Apparently, it occurs for $T \rightarrow 0$ and $\omega \rightarrow \omega_p$,

$$\nu_{\text{eff}}(n, T, \omega) \leq \nu_{\text{eff}}(n, 0, \omega_p(n)) \equiv \nu_{\text{eff}}^{\text{max}}(n). \quad (30)$$

There are two limiting cases, depending on density (see Fig. 5). For $\hat{T}_F \ll \hat{\omega}_p \ll 1$, corresponding to $n \ll 10^{24}\text{cm}^{-3}$ and asymptotic region V, Eq. (53) sets the maximum:

$$\nu_{\text{eff}}^{\text{max}}(n) \simeq \frac{4}{3\sqrt{3}} Z \nu_0 \frac{kT_F}{\hbar\omega_p} \propto n^{1/6}. \quad (31)$$

On the other hand, for $1 \ll \hat{\omega}_p \ll \hat{T}_F$, corresponding to $n \gg 10^{24}\text{cm}^{-3}$ and asymptotic region III, we find from Eq. (49)

$$\nu_{\text{eff}}^{\text{max}}(n) = \frac{4}{3\pi} Z \nu_0 \ln \frac{4kT_F}{\hbar\omega_p} \propto \ln n. \quad (32)$$

D. Z-scaling of ν_{eff}

The dependence of the collision frequency on ion charge Z is obtained from the hydrogen results $\nu_{\text{eff}}(\hbar\omega, kT, n; Z_H = 1)$ by making use of the scaling relation

$$\nu_{\text{eff}}(\hbar\omega, kT, n; Z) = Z \nu_{\text{eff}}(\hbar\omega/Z^2, kT/Z^2, n/Z^3; Z_H = 1). \quad (33)$$

This follows directly from Eq. (27): energies scale $\propto Z^2$, electron density $\propto Z^3$ due to Eq. (14), and ν_{eff} itself $\propto Z$. Of course, this holds only under the assumption that the plasma is fully ionized which requires sufficiently high temperature. With this in mind, one may apply these results also approximately to partially ionized plasma, replacing Z by an average ion charge Z_{av} to describe the free-free component of the total absorption, and determine bound-free and bound-bound components separately.

Z-scaling is illustrated in Fig. 7. In double logarithmic presentation, the plot pattern simply shifts with Z . Of course, the boundaries of validity vary differently: the relativistic limit for $\hbar\omega < mc^2$ and $kT < mc^2$ is invariant, and the lower limit on frequency varies according to $\hbar\omega_p \propto n^{1/2} \propto Z^{3/2}$.

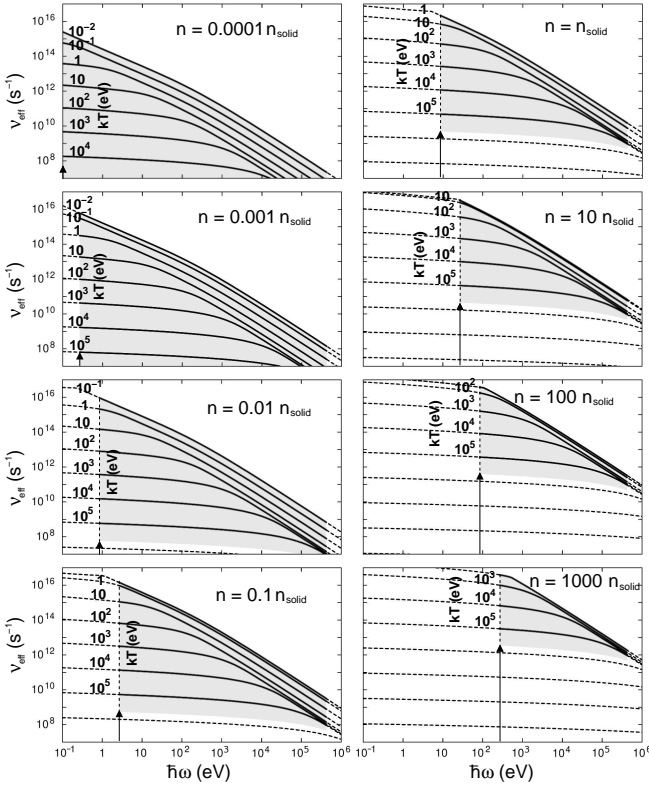


FIG. 6. Same as Fig. 4, but varying density from $10^{-4}n_0$ to 10^3n_0 . The black arrows mark the plasmon energy $\hbar\omega_p$. The shaded areas show the area of validity of the present theory; it is limited to non-relativistic temperatures $kT \leq mc^2$ and photon energies $\hbar\omega \leq mc^2$.

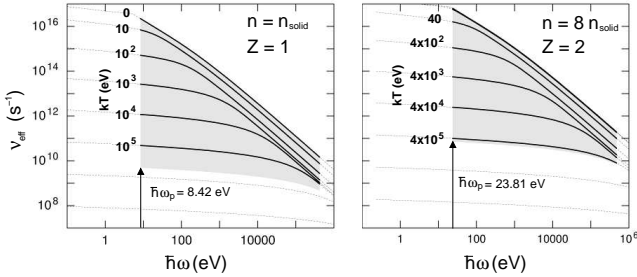


FIG. 7. Scaling of ν_{eff} with ion charge Z . Left: for $Z = 1$ and solid density; right: ν_{eff} for $Z = 2$ with scaled temperature ($kT \propto Z^2$), density ($n \propto Z^3$), and plasmon energy ($\hbar\omega_p \propto n^{1/2} \propto Z^{3/2}$).

IV. LIMITING REGIONS AND CORRESPONDING ANALYTICAL FORMULAS

The general formula Eq. (27) for ν_{eff} comprises a number of asymptotic regions, admitting various approximate formulas. The complexity arises because of the numerous different combinations of the external parameters: the photon frequency ω , the temperature T , and the electron density n . While n is a simple scaling parameter for non-degenerate high-temperature plasma (the cases studied in most of the astrophysical literature), the focus of the present work is on WDM at any degree of Fermi degeneracy, and therefore n enters through the Fermi temperature $kT_F = (\hbar^2/2m)(3\pi^2n)^{2/3}$ in a non-linear way and needs to be considered explicitly. In addition, we have to distinguish between slow ($\varepsilon < Z^2E_a$) and fast ($\varepsilon > Z^2E_a$) electrons, and this leads to the transitions from quasi-classical to quantum-mechanical behaviour seen in Fig. 1. It is important for WDM. In the following, we discuss some of these cases, in particular to explain features seen in Figs. 3 and 4. Concerning notation, we shall use both: normalized parameters $\hat{\varepsilon} = \varepsilon/(Z^2E_a)$, $\hat{\omega} = \omega/(Z^2E_a)$, $\hat{\mu} = \mu/(Z^2E_a)$, $\hat{T} = kT/(Z^2E_a)$, $\hat{T}_F = kT_F/(Z^2E_a) = (3\pi^2na_B^3)^{2/3}/(2Z^2)$, and also the corresponding dimensional ones, when convenient.

A. The Fermi degenerate electron gas ($kT \ll kT_F \sim \varepsilon$)

Concerning the target electron gas, the two temperature regions $kT \simeq 0$ and $kT \rightarrow \infty$ represent limiting situations. At zero temperature, the Fermi function takes the shape of the step function

$$f(p) = \begin{cases} 1 & (p < p_F) \\ 0 & (p > p_F) \end{cases} \quad (34)$$

extending at value unity from 0 to Fermi momentum

$$p_F = \hbar(3\pi^2n)^{1/3} \quad (35)$$

and vanishing elsewhere. The chemical potential then becomes

$$\mu = \varepsilon_F = kT_F = \frac{p_F^2}{2m} = \frac{\hbar^2}{2m}(3\pi^2n)^{2/3}, \quad (36)$$

defining the Fermi energy ε_F and the Fermi temperature T_F .

For temperatures larger than zero, the density integral Eq. (14) determining μ has to be inverted. The approximate solution

$$\frac{\mu}{kT} \simeq -\frac{3}{2} \ln \Theta + \ln \frac{4}{3\sqrt{\pi}} + \frac{P_1\Theta^{-(p_0+1)} + P_2\Theta^{-(p_0+1)/2}}{1 + P_1\Theta^{-p_0}} \quad (37)$$

was given by Ichimaru²⁶. Here $\Theta = T/T_F$, and the parameters $P_1 = 0.25054$, $P_2 = 0.072$, and $p_0 = 0.858$ have been adjusted to the exact result. The agreement with the exact result is better than 0.2%.

B. The high-temperature classical plasma ($kT_F \ll kT \sim \varepsilon$)

For temperatures much higher than the Fermi temperature, $T \gg T_F$, the distribution function approaches the Maxwellian distribution

$$f\left(\frac{\varepsilon - \mu}{kT}\right) = \frac{1}{e^{(\varepsilon - \mu)/kT} + 1} \approx \frac{4}{3\sqrt{\pi}} \left(\frac{T_F}{T}\right)^{3/2} e^{-\varepsilon/kT}. \quad (38)$$

For $T \rightarrow \infty$, the third term on the right-hand side of Eq. (37) vanishes, while the first two give the result Eq. (38).

High temperatures imply fast target electrons ($\hat{\varepsilon} > 1$), and we find from Eq. (28)

$$G(\hat{\varepsilon}, \hat{\omega}) \simeq \frac{1}{4\pi^2} \ln \frac{\sqrt{\hat{\varepsilon} + \hat{\omega}} + \sqrt{\hat{\varepsilon}}}{\sqrt{\hat{\varepsilon} + \hat{\omega}} - \sqrt{\hat{\varepsilon}}}. \quad (39)$$

Inserting Eqs. (38) and (39) into the integral (27), one obtains

$$\nu_{\text{eff}} = \frac{16}{9\pi^{3/2}} Z\nu_0 \left(\frac{T_F}{T}\right)^{3/2} L, \quad (40)$$

where

$$\begin{aligned} L &= \frac{(1 - e^{-\zeta})}{\zeta} \int_0^\infty \ln \left(\frac{\sqrt{x + \zeta} + \sqrt{x}}{\sqrt{x + \zeta} - \sqrt{x}} \right) e^{-x} dx \\ &= \frac{e^{\zeta/2} - e^{-\zeta/2}}{\zeta} K_0(\zeta/2); \end{aligned} \quad (41)$$

here $x = \varepsilon/kT$, $\zeta = \hbar\omega/kT$, and K_0 is the modified Bessel function of second kind and order zero.

C. Asymptotic limits in region I

Region I refers to 'slow' target electrons ($\hat{\varepsilon} \ll 1$) and high-energy photons ($\hat{\omega} \gg 1$). It contributes to ν_{eff} in Eq. (27) only for sufficiently small density such that $\hat{T}_F \ll 1$; this is the case e.g. for hydrogen plasma at solid density. In region I, one has $G(\hat{\varepsilon}, \hat{\omega}) \approx (\pi\sqrt{2\hat{\omega}})^{-1}$ (compare Table I), and the integral Eq. (27) can be solved analytically. Making use of

$$\int_0^\infty \frac{dx}{1 + e^{x+a}} = \ln(1 + e^{-a}), \quad (42)$$

we find

$$\nu_{\text{eff}} \simeq \frac{16\pi}{3} Z\nu_0 \frac{1}{\pi\sqrt{2\hat{\omega}}} \frac{\hat{T}}{\hat{\omega}} \ln \frac{1 + e^{\hat{\mu}/\hat{T}}}{1 + e^{(\hat{\mu} - \hat{\omega})/\hat{T}}}. \quad (43)$$

Here the denominator ($1 + \exp((\hat{\mu} - \hat{\omega})/\hat{T})$) under the logarithm in Eq. (43) approaches unity for $\hat{\omega} \gg 1$ so that we have

$$\nu_{\text{eff}} \simeq \frac{16}{3\sqrt{2}} Z\nu_0 \frac{\hat{T}}{\hat{\omega}^{3/2}} \ln(1 + \exp(\hat{\mu}/\hat{T})); \quad (44)$$

Combined with Eq. (37) for μ , this covers region I for any value of the degeneracy parameter $\Theta = T/T_F$. A comparison with the full numerical solution is given in Fig. 3 for 100 keV photons. For $T \rightarrow 0$, Eq. (44) becomes

$$\nu_{\text{eff}} = \frac{16}{3\sqrt{2}} Z\nu_0 \frac{\hat{T}_F}{\hat{\omega}^{3/2}} \quad (45)$$

and describes the upper boundary for ν_{eff} for sufficiently high photon energies in Fig. 4.

D. Asymptotic limits in region II

Region II refers to electron energies satisfying $1 \ll \hat{\varepsilon} \ll \hat{\omega}$, where $G(\hat{\varepsilon}, \hat{\omega}) \simeq (1/2\pi^2)\sqrt{\hat{\varepsilon}/\hat{\omega}}$ applies. The integral in Eq. (27) then reduces essentially to the density integral $\int d\hat{\varepsilon} \sqrt{\hat{\varepsilon}} f((\hat{\varepsilon} - \hat{\mu})/\hat{T}) = (2/3)\hat{T}_F^{3/2} \propto n$ (see Eq. (14)), and we find

$$\nu_{\text{eff}} \simeq \frac{16}{9\pi} Z\nu_0 \left(\frac{\hat{T}_F}{\hat{\omega}}\right)^{3/2}. \quad (46)$$

Notice that ν_{eff} becomes independent of temperature. Such a tendency is clearly observed in Fig. 3 and is responsible for the clustering at the lower boundary of the strip of isotherms in Fig. 4. One may also notice that Eq. (46) holds for both classical plasma in the range $1 \ll \hat{T} \ll \hat{\omega}$ and degenerate plasma, occurring at high densities for $1 \ll \hat{T}_F \ll \hat{\omega}$.

E. Asymptotic limits in region III

We now turn to temperatures much larger than the photon energy, such that $\hat{\omega} \ll \hat{\varepsilon}$. In this limit, the integral Eq. (IV B) becomes $L = \ln(4/\zeta) - \gamma$, where $\gamma = 0.577$ is Euler's constant, and one obtains

$$\nu_{\text{eff}} = \frac{4\sqrt{2\pi}}{3} \frac{Zne^4}{\sqrt{m}(kT)^{3/2}} \left(\ln \frac{4kT}{\hbar\omega} - \gamma \right). \quad (47)$$

Here we have expressed the Fermi temperature Eq. (36) in Eq. (40) by the elementary quantities to recover Spitzer's formula Eq. (2) in its well known form. The front factor is identical to what is found in standard text books (see e.g. Ref. 27), and the logarithmic term reproduces the quantum Coulomb logarithm of Bethe in the limit $\omega \rightarrow \omega_p$.²⁸ In Fig. 3, Eq. (47) is seen to provide the upper boundary of ν_{eff} for sufficiently high temperature.

At sufficiently high density, the Fermi temperature kT_F becomes larger than the plasmon energy $\hbar\omega_p$, and light may propagate in degenerate plasma ($1 \ll \hat{\omega}_p \leq \hat{\omega} \ll \hat{T}_F$ and $\hat{T} \ll \hat{T}_F$). The integral Eq. (27) is then performed over step-like distribution functions:

$$\nu_{\text{eff}} \simeq \frac{16\pi}{3} Z\nu_0 \frac{1}{4\pi^2} \left[\int_{kT_F - \hbar\omega}^{kT_F} \ln \frac{\sqrt{\varepsilon + \hbar\omega} + \sqrt{\varepsilon}}{\sqrt{\varepsilon + \hbar\omega} - \sqrt{\varepsilon}} \frac{d\varepsilon}{\hbar\omega} \right]; \quad (48)$$

here the lower boundary of the integral indicates that only electrons with energy $\varepsilon > kT_F - \hbar\omega$ contribute to absorption due to the Pauli principle, and we find

$$\nu_{\text{eff}} = \frac{4}{3\pi} Z\nu_0 \ln \frac{4\hat{T}_F}{\hat{\omega}}. \quad (49)$$

F. Asymptotic limit for region IV

For sufficiently low density (such that $\hat{T}_F \ll 1$), an additional asymptotic regime is found in region IV, where $\hat{T}_F \ll \hat{\omega}_p \leq \hat{\omega} \ll \varepsilon^{3/2} < 1$ holds. This corresponds to a non-degenerate plasma with Maxwellian electron distribution. Using the approximate expression for $G(\hat{\varepsilon}, \hat{\omega})$, valid for region IV (see Table I), Eq. (27) for ν_{eff} takes the form

$$\begin{aligned} \nu_{\text{eff}} &= \frac{16}{9\pi^{3/2}} Z\nu_0 \left(\frac{\hat{T}_F}{\hat{T}}\right)^{3/2} \frac{1 - e^{-\hat{\omega}/\hat{T}}}{\hat{\omega}/\hat{T}} \\ &\times \int_0^\infty \left(\ln \frac{4\sqrt{2}\hat{\varepsilon}^{3/2}}{\hat{\omega}} - \gamma\right) \exp\left(-\frac{\hat{\varepsilon}}{\hat{T}}\right) \frac{d\hat{\varepsilon}}{\hat{T}}. \end{aligned} \quad (50)$$

Recalling $\int_0^\infty \ln x e^{-x} dx = -\gamma$, one gets

$$\nu_{\text{eff}} = \frac{4\sqrt{2}\pi}{3} \frac{Zne^4}{\sqrt{m}(kT)^{3/2}} \left(\ln \frac{4\sqrt{2}(kT)^{3/2}}{Ze^2\omega\sqrt{m}} - \frac{5}{2}\gamma\right). \quad (51)$$

This result is similar to Eq. (47), but under the logarithm it shows the parametric combination $T^{3/2}/(Z\omega)$ characteristic for Bohr's classical Coulomb logarithm in contrast to Bethe's quantum-mechanical result $\propto \ln(4kT/\hbar\omega)$ (see e.g. Ref. 1). So even the transition between the classical and quantum Coulomb logarithms is contained in the present formalism and naturally emerges under the appropriate limit. For solid-density hydrogen, region VI is just marginally touched (compare line *a* in Fig. 2) and does not clearly show up in Fig. 3.

G. Asymptotic limit in region V

This region is defined by the condition $\hat{\varepsilon}^{3/2} \ll \hat{\omega} \ll 1$. Here $G(\hat{\varepsilon}, \hat{\omega}) \approx 1/(4\pi\sqrt{3})$ (compare Table I) is independent of $\hat{\varepsilon}$ as in region I, and one obtains

$$\nu_{\text{eff}} \simeq \frac{4}{3\sqrt{3}} Z\nu_0 \frac{\hat{T}}{\hat{\omega}} \ln \frac{1 + \exp(\hat{\mu}/\hat{T})}{1 + \exp((\hat{\mu} - \hat{\omega})/\hat{T})}. \quad (52)$$

There exist a number of sublimits here; however, it may be best to use the full Eq. (52) in combination with Eq. (37). In the limit $\hat{T} \rightarrow 0$ and $\hat{\omega} \rightarrow \hat{\omega}_p \gg T_F$,

$$\nu_{\text{eff}} \simeq \frac{4}{3\sqrt{3}} Z\nu_0 \frac{\hat{T}_F}{\hat{\omega}_p}; \quad (53)$$

it depends only on density and scales $\propto n^{1/6}$. It describes the maximum value of ν_{eff} in Fig. 6 for a given density well below the solid density.

V. SUMMARY AND OUTLOOK

Collisional free-free photon absorption in dense plasma has been studied with particular focus on warm dense matter. A global expression for the effective collision frequency $\nu_{\text{eff}}(T, \hbar\omega, n)$ has been derived from Sommerfeld's cross section for bremsstrahlung. It holds for frequencies above the plasma frequency and in the non-relativistic regime. Numerical results for fully ionized hydrogen plasma at solid density are presented over a wide range of temperatures T and photon energies $\hbar\omega$. Also the dependence on density n is obtained over a wide range, covering any degree of degeneracy. For ions with charge number $Z > 1$, the relation for Z -scaling is derived.

We have identified a number of asymptotic regions in which the numerical results can be represented by simple analytical formulas. For sufficiently high temperatures and $\hbar\omega \ll kT$, Spitzer's formula for a classical plasma is reproduced and appears as an upper bound to ν_{eff} . Concerning scaling with frequency, $\nu_{\text{eff}} \propto \omega^{-3/2}$ is found for temperatures $kT \ll \hbar\omega$, independent of the degree of degeneracy; it leads to the free-free opacity scaling $\kappa \propto \omega^{-7/2}$, well-known in astrophysics. For intermediate regions, relevant to warm dense matter, new asymptotic relations are found that should be tested experimentally.

The present results are based on the quantum-mechanical solution of radiant electron collisions with ions. The most difficult part of the work has been the numerical evaluation of the hypergeometric functions involved. This problem has been investigated independently in the astrophysical literature, calculating the free-free Gaunt factor. The methods used in the present work are outlined in the Appendices.

For applications, it is planned, in a companion paper, to provide a global fit formula, based on the present work and sufficiently accurate for direct use in numerical codes.

ACKNOWLEDGEMENTS

R. R. acknowledges the hospitality of the Max-Planck-Institut für Quantenoptik, where most of the present work was done, and financial support from the Spanish Ministerio de Economía y Competitividad, Project No. ENE2014-54960-R, and by the EUROfusion Consortium under the project AWP15-ENR-01/CEA-02. J. MtV thanks Stefanie Hansen and Peter Mulser for advice concerning evaluations of the Gaunt factor in the astrophysical literature and also for discussions with Thomas Blenski on photo-absorption in dense plasma.

Appendix A: Numerical evaluation of $G(\hat{\varepsilon}, \hat{\omega})$

The numerical evaluation of the kernel $G(\hat{\varepsilon}, \hat{\omega})$ is not trivial due to the presence of hypergeometric functions. As such functions are not available in standard libraries

for all possible combinations of large/small values of the arguments, numerical techniques tailored for each specific problem are frequently required²⁹. Here, in order to be close to literature standards^{21,23,30}, we introduce a notation slightly different from the one used in the main text, namely, $\nu \equiv \eta_+$ and $\nu' \equiv \eta$. Eq. (23) now takes the form

$$G(\hat{\varepsilon}, \hat{\omega}) = \frac{\xi}{4} \frac{d|F(i\nu', i\nu; 1; \xi)|^2/d\xi}{(1 - e^{-2\pi\nu'})(e^{2\pi\nu} - 1)}, \quad (\text{A1})$$

where

$$\nu = \frac{1}{\sqrt{2(\hat{\varepsilon} + \hat{\omega})}}, \quad \nu' = \frac{1}{\sqrt{2\hat{\varepsilon}}}, \quad \xi = -\frac{4\nu\nu'}{(\nu - \nu')^2}. \quad (\text{A2})$$

The derivative in Eq. (A1) can be expressed as (Eq. (15.5.1) of Ref. 20)

$$\frac{d}{d\xi}|F(i\nu', i\nu; 1; \xi)|^2 = 2\Re \left[F^*(i\nu', i\nu; 1; \xi) \frac{d}{d\xi} F(i\nu', i\nu; 1; \xi) \right], \quad \text{where} \quad (\text{A3})$$

$$\frac{d}{d\xi} F(i\nu', i\nu; 1; \xi) = -\nu\nu' F(1 + i\nu', 1 + i\nu; 2; \xi). \quad (\text{A4})$$

Hypergeometric functions are defined by Gauss series (Eq. (15.2.1) of Ref. 20)

$$F(a, b; c; \xi) = 1 + \frac{ab}{c} \frac{\xi}{1!} + \frac{a(a+1)b(b+1)}{c(c+1)} \frac{\xi^2}{2!} + \dots \quad (\text{A5})$$

on the disk $|\xi| < 1$, and by analytic continuation elsewhere. In our case, ξ is always real and negative. For $\xi \leq -1$, one can use the expression (Eq. (15.3.8) of Ref. 19)

$$F(a, b; c; \xi) =$$

$$\begin{aligned} & \frac{\Gamma(c)\Gamma(b-a)}{\Gamma(b)\Gamma(c-a)} (1-\xi)^{-a} F\left(a, c-b; a-b+1; \frac{1}{1-\xi}\right) \\ & + \frac{\Gamma(c)\Gamma(a-b)}{\Gamma(a)\Gamma(c-b)} (1-\xi)^{-b} F\left(b, c-a; b-a+1; \frac{1}{1-\xi}\right), \end{aligned} \quad (\text{A6})$$

that maps the interval $\xi \in (-\infty, -1)$ into the interval $(0, 1/2)$, where the series converge. Gamma functions of complex arguments have been evaluated by the algorithm described in Sec. 6.1 of Ref. 31. For $-1 \leq \xi < 0$, we use (Eq. (15.3.4) of Ref. 19)

$$F(a, b; c; \xi) = (1-\xi)^{-a} F\left(a, c-b; c; \frac{\xi}{\xi-1}\right), \quad (\text{A7})$$

that maps the interval $\xi \in (-1, 0)$ into the interval $(0, 1/2)$, ensuring fast convergence of the series even if ξ is close to -1 . However, severe cancellation errors prevent the use of Eqs. (A) and (A7) for large values of the parameters (e.g., for $\nu/\nu' = 1/2$ and double precision

arithmetic, Eq. (A) fails for $\nu' \gtrsim 250$). To overpass this difficulty, arbitrary precision floating point arithmetic was used by van Hoof et al.¹⁵. Here, we apply a different approach, using the following integral representation (Eq. (15.6.1) of Ref. 20)

$$F(a, b; c; \xi) = \frac{\Gamma(c)}{\Gamma(b)\Gamma(c-b)} \int_0^1 \frac{t^{b-1}(1-t)^{c-b-1}}{(1-\xi t)^a} dt, \quad (\text{A8})$$

$\Re c > \Re b > 0,$

where, $a = i\nu'$, $b = i\nu$, and $c = 1$. Defining $\rho = \nu/\nu'$ and using the ‘‘reflection formula’’ $\Gamma(z)\Gamma(1-z) = \pi/\sin \pi z$ (Eq. (5.5.3) of Ref. 20), one gets

$$F(i\nu', i\rho\nu'; 1, \xi) = \frac{i \sinh(\pi\rho\nu')}{\pi} I, \quad (\text{A9})$$

$$I = \int_0^1 t^{i\rho\nu'-1} (1-t)^{-i\rho\nu'} (1-\xi t)^{-i\nu'} dt \quad (\text{A10})$$

The requirement $\Re b > 0$ is not satisfied, but, because hypergeometric functions are continuous in the parameters, we can evaluate the integral for $b = i\rho\nu' + \varsigma$ (ς real and positive), and afterwards take the limit $\varsigma \rightarrow 0$. The derivative of F is obtained by taking the derivative of the integrand of Eq. (A9) with respect to ξ

$$\frac{d}{d\xi} F(i\nu', i\rho\nu'; 1; \xi) = -\frac{\nu' \sinh(\pi\rho\nu')}{\pi} I_A, \quad (\text{A11})$$

where

$$I_A = \int_0^1 t^{i\rho\nu'-1} (1-t)^{-i\rho\nu'} (1-\xi t)^{-i\nu'-1} dt. \quad (\text{A12})$$

Direct application of these expressions in Eq. (A1) can cause also cancellation problems for large ν and ν' . These can be overcome by evaluating

$$I_B = I - \left(\frac{2}{1-\rho} - \xi \right) I_A =$$

$$\int_0^1 \left(\frac{1}{t} - \frac{2}{1-\rho} \right) t^{i\rho\nu'-1} (1-t)^{-i\rho\nu'} (1-\xi t)^{-i\nu'-1} dt \quad (\text{A13})$$

instead of I . Finally Eq. (A1) takes the form

$$G = \frac{\nu' |\xi|}{16\pi^2} \frac{1 - e^{-2\pi\nu}}{1 - e^{-2\pi\nu'}} |I_A I_B^* - I_A^* I_B|. \quad (\text{A14})$$

The methods used to evaluate numerically the integrals I_A and I_B are described in Appendix C.

Appendix B: Asymptotic limits of $G(\hat{\epsilon}, \hat{\omega})$

The asymptotic limits of the Sommerfeld cross section have been widely studied^{6,21–23,32}. However, the derivations of particular cases are rather scattered through the literature, frequently using different notations and normalization factors. For this reason, we introduce in this appendix a systematic derivation of the five asymptotic limits displayed in table 1. It should be mentioned that we could not find, in the literature, an asymptotic limit valid for the full domain III-IV, similar to the one derived below. As indicated in Appendix A, the hypergeometric functions that appear in $G(\hat{\epsilon}, \hat{\omega})$ can be evaluated in three different ways, namely either using Eq. (A5), Eq. (A), or Eq. (A9). In one to one correspondence with these three ways, three asymptotic limits for $G(\hat{\epsilon}, \hat{\omega})$ have been derived.

1. Regions I and II

If $|\xi| < 1$ and $\nu \ll 1$, the power expansion in Eq. (A4) simplifies to

$$\begin{aligned} \frac{d}{d\xi} F(i\nu', i\nu; 1; \xi) &= \\ -\nu\nu' F(1 + i\nu', 1 + i\nu; 2; \xi) &\simeq -\nu\nu' F(1 + i\nu', 1; 2; \xi) = \\ -\nu\nu' \left(1 + \frac{(1 + i\nu')}{2} \frac{\xi}{1!} + \frac{(1 + i\nu')(2 + i\nu')}{3} \frac{\xi^2}{2!} + \dots \right). & \end{aligned} \quad (\text{B1})$$

Notice that if $\nu' \sim \nu \ll 1$, the simplified series becomes $\sum_{n=0}^{\infty} \xi^n / (1+n) = -\ln(1-\xi)/\xi$. On the other hand, if $\nu' \gg \nu$, then $|\xi| = 4\nu\nu' / (\nu - \nu')^2 \simeq 4\nu/\nu' \ll 1$, and all ξ power terms in Eq. (B1) can be neglected, so that $F(1 + i\nu', 1; 2; \xi) \simeq 1 = -\lim_{\xi \rightarrow 0} \ln(1-\xi)/\xi$. This leads in both cases to

$$\frac{d}{d\xi} F(i\nu', i\nu; 1; \xi) \simeq \nu\nu' \frac{\ln(1-\xi)}{\xi}. \quad (\text{B2})$$

The hypergeometric function itself can be evaluated by integration

$$\begin{aligned} F(i\nu', i\nu; 1; \xi) &= F(i\nu', i\nu; 1; 0) + \int_0^\xi \frac{d}{d\xi} F(i\nu', i\nu; 1; \xi) d\xi \simeq \\ 1 + \nu\nu' \int_0^\xi \frac{\ln(1-\xi)}{\xi} d\xi &\simeq 1. \end{aligned} \quad (\text{B3})$$

For $|\xi| < 1$, the integrand is bounded $|\ln(1-\xi)/\xi| \leq 1$, so that the absolute value of the second term in Eq. (B1) is less than $|\nu\nu'\xi| \sim \nu^2 \ll 1$ and can be neglected. Using Eqs. (B1) and (B1) in Eq. (A1), one gets

$$G \simeq \frac{1}{2\pi} \frac{\nu'}{1 - e^{-2\pi\nu'}} \ln \frac{\nu' + \nu}{\nu' - \nu} =$$

$$\frac{1}{2\pi} \frac{1/\sqrt{2\hat{\epsilon}}}{1 - e^{-2\pi/\sqrt{2\hat{\epsilon}}}} \ln \frac{\sqrt{\hat{\epsilon} + \hat{\omega}} + \sqrt{\hat{\epsilon}}}{\sqrt{\hat{\epsilon} + \hat{\omega}} - \sqrt{\hat{\epsilon}}}. \quad (\text{B4})$$

In terms of $\hat{\epsilon}$ and $\hat{\omega}$, the conditions $\nu \ll 1$ and $|\xi| < 1$ become $\hat{\epsilon} + \hat{\omega} \gg 1$ and $\hat{\omega} > 4(4 + 3\sqrt{2})\hat{\epsilon}$, respectively. So Eq. (B1) is valid deeply inside the joint regions marked as I and II in Fig. 2.

2. Regions III and IV

For $|\xi| > 1$, the Taylor series in Eqs. (A5) diverges, and one must use Eq. (A). In that case, it proves convenient to introduce the auxiliary variables $\epsilon = \frac{1}{2}(\nu' - \nu)$, $\bar{\nu} = \frac{1}{2}(\nu' + \nu)$. Here, we assume that $\epsilon \ll 1$ and $\epsilon \ll \bar{\nu}$ (although $\bar{\nu}$ can be arbitrary). With $a = i(\bar{\nu} + \epsilon)$, $b = i(\bar{\nu} - \epsilon)$, and $c = 1$, Eq. (A) takes the form

$$\begin{aligned} F(i\nu', i\nu; 1; \xi) &= \frac{\Gamma(-2i\epsilon)}{\Gamma(i(\bar{\nu} - \epsilon))\Gamma(1 - i(\bar{\nu} + \epsilon))} (1 - \xi)^{-i(\bar{\nu} + \epsilon)} \\ &\times F\left(i(\bar{\nu} + \epsilon), 1 - i(\bar{\nu} - \epsilon); 1 + 2i\epsilon; \frac{1}{1 - \xi}\right) \\ &+ \frac{\Gamma(2i\epsilon)}{\Gamma(i(\bar{\nu} + \epsilon))\Gamma(1 - i(\bar{\nu} - \epsilon))} (1 - \xi)^{-i(\bar{\nu} - \epsilon)} \\ &\times F\left(i(\bar{\nu} - \epsilon), 1 - i(\bar{\nu} + \epsilon); 1 - 2i\epsilon; \frac{1}{1 - \xi}\right). \end{aligned} \quad (\text{B5})$$

Due to $\Gamma(0) = \infty$, the two terms are singular for $\epsilon \rightarrow 0$ with opposite sign. Thus, to evaluate this expression for $\epsilon \ll 1$, it is necessary to expand each term in powers of ϵ up to first order. The hypergeometric functions, having a small argument $1/(1-\xi) = \epsilon^2/\bar{\nu}^2$, can be expressed as fast convergent series

$$\begin{aligned} F(i(\bar{\nu} \pm \epsilon), 1 - i(\bar{\nu} \mp \epsilon), 1 \pm 2i\epsilon, \frac{\epsilon^2}{\bar{\nu}^2}) &= \\ 1 + \frac{i(\bar{\nu} \pm \epsilon)(1 - i(\bar{\nu} \mp \epsilon))}{1 \pm 2i\epsilon} \frac{\epsilon^2}{\bar{\nu}^2} + \dots & \end{aligned} \quad (\text{B6})$$

As $\epsilon \ll \min(1, \bar{\nu})$, the leading term of the series is either of order ϵ^2 , if $\bar{\nu} \gg 1$, or of order $\epsilon^2/\bar{\nu}$, if $\bar{\nu} \ll 1$. In both cases, it can be neglected in comparison with terms of order ϵ , and one may set $F = 1$ in the right hand side of Eq. (B2). The factors containing the gamma functions can be simplified using the identities (Eqs. (5.4.1), (5.5.1), and (5.5.3) of Ref. 20) $\Gamma(1) = 1$, $z\Gamma(z) = \Gamma(z+1)$, $\Gamma(z)\Gamma(1-z) = \pi/\sin(\pi z)$, $\sin(iz) = i\sinh(z)$, and the Taylor expansion

$$\Gamma(z + \Delta z) = \Gamma(z) + \Gamma'(z)\Delta z + \dots = \Gamma(z)(1 + \psi(z)\Delta z + \dots), \quad (\text{B7})$$

where $\psi(z) \equiv \Gamma'(z)/\Gamma(z)$ is the psi (digamma) function (Eq. (5.2.2) of Ref. 20). Retaining terms up to first order in ϵ ;

$$F(i\nu', i\nu; 1; \xi) \simeq \frac{\bar{\nu} \sinh(\pi\bar{\nu})}{\epsilon} (1-\xi)^{-i\bar{\nu}} \times \left(-\frac{1+2i\epsilon a(\bar{\nu})}{\bar{\nu}+\epsilon} (1-\xi)^{-i\epsilon} + \frac{1-2i\epsilon a(\bar{\nu})}{\bar{\nu}-\epsilon} (1-\xi)^{i\epsilon} \right), \quad (\text{B8})$$

where we introduce the function $a(\bar{\nu}) \equiv -\psi(1) + \frac{1}{2}(\psi(i\bar{\nu}) + \psi(-i\bar{\nu}))$. From this expression, it is straightforward to obtain

$$\frac{d|F|^2}{d\xi} \simeq \frac{\sinh^2(\pi\bar{\nu})}{\pi^2(\bar{\nu}^2 - \epsilon^2)} \epsilon (4\epsilon a(\bar{\nu}) \cos(2\epsilon \ln(1-\xi)) - (1 - 4\epsilon^2 a(\bar{\nu})^2) \sin(2\epsilon \ln(1-\xi))), \quad (\text{B9})$$

and, taking into account that $\epsilon \ll \bar{\nu} \simeq \nu \simeq \nu'$ and $\epsilon \ll 1$,

$$\frac{d|F|^2}{d\xi} \simeq \frac{4 \sinh^2(\pi\nu')}{\pi^2 \xi} \left(\ln \frac{\nu'}{\epsilon} - a(\nu') \right). \quad (\text{B10})$$

Finally, using this expression in Eq. (A1), one gets

$$G \simeq \frac{1}{4\pi^2} \left(\ln \frac{2\nu'}{\nu' - \nu} - a(\nu') \right) \simeq \frac{1}{4\pi^2} \left(\ln \frac{4\hat{\epsilon}}{\hat{\omega}} - a(1/\sqrt{2\hat{\epsilon}}) \right). \quad (\text{B11})$$

Although function $a(\bar{\nu})$ contains the special function $\psi(\bar{\nu})$, using Eq. (5.7.6) of Ref. 20, it can be transformed into a form suitable for efficient numerical evaluation

$$a(\bar{\nu}) = \bar{\nu}^2 \sum_{n=1}^{\infty} \frac{1}{n(n^2 + \bar{\nu}^2)} \simeq$$

$$\bar{\nu}^2 \sum_{n=1}^N \frac{1}{n(n^2 + \bar{\nu}^2)} + \frac{1}{2} \ln \left(\frac{\bar{\nu}^2}{(N+1/2)^2} + 1 \right). \quad (\text{B12})$$

For $N = 100$, $a(\bar{\nu})$ is obtained with a relative error less than 10^{-6} for any positive value of $\bar{\nu}$. For small and large arguments, using Eqs. (5.4.12), (5.11.2), and (25.2.1) of Ref. 20, one has

$$a(\bar{\nu}) \simeq \begin{cases} \zeta(3)\bar{\nu}^2 & \text{for } \bar{\nu} \ll 1 \\ \gamma + \ln \bar{\nu} & \text{for } \bar{\nu} \gg 1 \end{cases} \quad (\text{B13})$$

where $\zeta(3) = 1.20205\dots$ is Apéry's constant (ζ is the Riemann Zeta function) and $\gamma = 0.57721\dots$ is Euler's

constant. Eq. (B11) has been derived under the assumption $\epsilon \ll \min(1, \bar{\nu})$, which can be written as

$$\sqrt{\hat{\epsilon} + \hat{\omega}} - \sqrt{\hat{\epsilon}} \ll \min(\sqrt{\hat{\epsilon}}\sqrt{\hat{\epsilon} + \hat{\omega}}, \sqrt{\hat{\epsilon} + \hat{\omega}} + \sqrt{\hat{\epsilon}}). \quad (\text{B14})$$

This is only possible if $\hat{\omega} \ll \hat{\epsilon}$. In that case, Eq. (B14) becomes $\hat{\omega} \ll \min(\hat{\epsilon}, \hat{\epsilon}^{3/2})$, and it is satisfied in the regions marked as III and IV in Fig. 2.

3. Region V

This situation corresponds to the quasi-classical limit and has been treated in §92 of Ref. 21. Here we obtain the asymptotic limit from Appendix A. The integrals defined by Eqs. (A12) and (A) can be written as

$$\int_0^1 g(t) e^{i\nu' f(t)} dt, \quad (\text{B15})$$

where $f(t)$ and $g(t)$ are real functions: $f(t) = \rho \ln t - \rho \ln(1-t) - \ln(1-\xi t)$ in both integrals. For large values of ν' , the integrands are strongly oscillating functions of t . The function $f(t)$ has a ‘‘saddle-point’’ at $t = t_0 \equiv (1-\rho)/2$, where the first and second derivatives of f are zero ($f'(t_0) = f''(t_0) = 0$). For large values of ν' , most of the integral value comes from the contribution in a small region around t_0 . This allows to consider only the leading terms in the Taylor's expansion of f and g around t_0 ; that is, $f(t) \simeq f(t_0) + \frac{1}{6} f'''(t_0)(t-t_0)^3$, and $g(t) \simeq g(t_0) + g'(t_0)(t-t_0)$, so that the integration interval can be extended from $-\infty$ to ∞ . Using Eqs. (5.9.6) and (5.9.7) of Ref. 20, these integrals become

$$I_A \simeq \left(\frac{1-\rho}{1+\rho} \right)^{1+i\nu'(1+\rho)} \left(\frac{(1-\rho^2)^2}{16\rho\nu'} \right)^{1/3} \frac{2\pi}{3^{2/3}\Gamma(\frac{2}{3})}, \quad (\text{B16})$$

$$I_B \simeq -\frac{4i}{(1-\rho)^2} \left(\frac{1-\rho}{1+\rho} \right)^{1+i\nu'(1+\rho)} \left(\frac{(1-\rho^2)^2}{16\rho\nu'} \right)^{2/3} 3^{1/6}\Gamma(\frac{2}{3}). \quad (\text{B17})$$

Using these values in Eq. (A14), one obtains

$$G \simeq \frac{1}{4\pi\sqrt{3}}. \quad (\text{B18})$$

This procedure can be justified only if the neglected terms in the expansions are small in the region around the ‘‘saddle-point’’ where $\nu'(f(t) - f(t_0)) \sim 1$. This condition can be written as $\nu \gg 1/(1-\rho)$ and, in terms of normalized quantities, as $\hat{\epsilon}^{3/2} \ll \hat{\omega} \ll 1$. It is satisfied for region V in Fig. 2.

4. Summary of asymptotic expressions

Summarizing the finding of Appendix B (Eqs. (B1), (B11), and (B18)), we have

$$G(\hat{\varepsilon}, \hat{\omega}) \simeq \frac{1}{2\pi} \frac{1/\sqrt{2\hat{\varepsilon}}}{1 - e^{-2\pi/\sqrt{2\hat{\varepsilon}}}} \ln \frac{\sqrt{\hat{\varepsilon} + \hat{\omega}} + \sqrt{\hat{\varepsilon}}}{\sqrt{\hat{\varepsilon} + \hat{\omega}} - \sqrt{\hat{\varepsilon}}} \simeq \begin{cases} \frac{1}{\pi\sqrt{2\hat{\omega}}} & (\text{Region I : } \hat{\omega} \gg 1 \gg \hat{\varepsilon}) \\ \frac{1}{2\pi^2} \sqrt{\frac{\hat{\varepsilon}}{\hat{\omega}}} & (\text{Region II : } \hat{\omega} \gg \hat{\varepsilon} \gg 1) \end{cases} \quad (\text{B19})$$

$$G(\hat{\varepsilon}, \hat{\omega}) \simeq \frac{1}{4\pi^2} (\ln \frac{4\hat{\varepsilon}}{\hat{\omega}} - a(1/\sqrt{2\hat{\varepsilon}})) \simeq \begin{cases} \frac{1}{4\pi^2} \ln \frac{4\hat{\varepsilon}}{\hat{\omega}} & (\text{Region III : } \hat{\omega} \ll \hat{\varepsilon}, 1 \ll \hat{\varepsilon}) \\ \frac{1}{4\pi^2} \ln \frac{4\sqrt{2}\hat{\varepsilon}^{3/2}}{\hat{\omega}e^\gamma} & (\text{Region IV : } \hat{\omega} \ll \hat{\varepsilon}^{3/2} \ll 1) \end{cases} \quad (\text{B20})$$

$$G(\hat{\varepsilon}, \hat{\omega}) \simeq \frac{1}{4\pi\sqrt{3}} \quad (\text{Region V : } \hat{\varepsilon}^{3/2} \ll \hat{\omega} \ll 1) \quad (\text{B21})$$

It is noteworthy that the asymptotic expression for region III, is also contained in Eq. (B1), despite the fact that Eq. (B1) can only be justified in regions I and II. Therefore Eq. (B1) applies to regions I, II, and III.

Appendix C: Numerical evaluation of integrals

The integral in Eq. (27) has the form

$$\int_0^\infty G\left(\frac{\varepsilon}{Z^2 E_a}, \frac{\hbar\omega}{Z^2 E_a}\right) \left[\frac{1}{1 + e^{\frac{\varepsilon - \mu}{kT}}} - \frac{1}{1 + e^{\frac{\varepsilon + \hbar\omega - \mu}{kT}}} \right] d\varepsilon. \quad (\text{C1})$$

For fixed ω and Z , the function G is finite for $\varepsilon = 0$, and grows logarithmically for large ε . The term in square brackets is maximum for $\varepsilon = \varepsilon_m \equiv \max(0, \mu - \frac{1}{2}\hbar\omega)$, and decreases exponentially ($\propto e^{-\varepsilon/kT}$) for large ε . Consequently, the upper integration limit can be set to $\varepsilon_m + 100 kT$ with negligible numerical error. The integration is carried out using an adaptive algorithm. The integration interval is decomposed into subintervals. In each subinterval, the integral and the numerical error are evaluated simultaneously. The subinterval with larger absolute error is halved into two smaller subintervals. This process is repeated until the global error estimate is below a given bound (in this work, a relative accuracy of 10^{-6}). For smooth real functions (like the ones in Eq. (27)), the subinterval quadrature is done using the composite Simpson's rule with five points (Eq. (3.5.7) of Ref. 20), and the numerical error is obtained as the difference between quadratures with five and with three points.

A modified version of the above algorithm has been applied to evaluate the complex integrals Eqs. (A12) and (A). Notice that, in both integrals, the integrand is singular at $t = 0$ and at $t = 1$. In the first subinterval $[0, h]$ ($h \ll 1$), the integrand can be approximated using a truncated Taylor series

$$(1-t)^{-i\nu\nu'} (1-\xi t)^{-i\nu'-1} = 1 + g_1 t + g_2 t^2 + g_3 t^3 + \dots + g_N t^N, \quad (\text{C2})$$

and the integration is then carried out term by term. When this expression is applied to Eq. (A), the first term in the series gives place to the improper integral $\int_0^h t^{i\rho\nu'-1} dt$. In that case, as it was explained in Appendix A, we have to take the limit: $\lim_{\varsigma \rightarrow 0} \int_0^h t^{i\rho\nu'+\varsigma-1} dt = h^{i\rho\nu'} / (i\rho\nu')$. As an estimate of the error, one can use the contribution coming from the last term in Eq. (C2). The same procedure can be applied to the last subinterval $[1-h, 1]$. For moderate values of ν' , Simpson's quadrature can be used for the rest of subintervals. However, for large values of ν' , the integrand is a fast oscillatory function of t , and the use of the Simpson's quadrature would require a prohibitive large number of function evaluations. To overcome this limitation, in each internal subinterval $[t_i, t_{i+1}]$, the complex integrand is approximated as

$$f(t) \simeq \bar{f}(u) \equiv (A + Bu + Cu^2)e^{i(D+Eu)}, \quad (\text{C3})$$

where u is a local variable ranging from zero (at t_i) to one (at t_{i+1}), related to t by

$$\frac{t - t_i}{t_{i+1} - t_i} = (1 - F)u + Fu^2. \quad (\text{C4})$$

The six real constants A to F are determined by the condition $\bar{f} = f$ at points t_i , $\frac{1}{2}(t_i + t_{i+1})$, and t_{i+1} . The integral across the subinterval can be evaluated in terms of elemental integrals

$$\int_{t_i}^{t_{i+1}} f(t) dt \simeq \int_{t_i}^{t_{i+1}} \bar{f}(u(t)) dt = (t_{i+1} - t_i) e^{iD} \times \int_0^1 (A + Bu + Cu^2)((1 - F) + 2Fu) e^{iEu} du. \quad (\text{C5})$$

Notice that, if $E \gg 1$, a large number of oscillations occurs between t_i and t_{i+1} . In each subinterval, the numerical error is evaluated as the difference between direct application of Eq. (C) and the sum of values obtained by dividing the subinterval in two halves.

- ¹S. Atzeni and J. Meyer-ter-Vehn, *The Physics of Inertial Fusion* (Oxford Science Publications, Oxford, 2004).
- ²P. A. Norreys and R. P. Drake, *New J. Phys.* **16**, 065007 (2014).
- ³Stanford XFEL: <https://lcls.slac.stanford.edu/lcls-ii/science>.
- ⁴DESY XFEL: <https://www.xfel.eu/science>.
- ⁵P. Holleb, O. Ciricosta, M. Desjarlais, C. Cacho, C. Spindloe, E. Springate, I. Turcu, J. Warrk, and S. Vinko, to appear in *Phys. Rev. E* (2018).
- ⁶A. Sommerfeld, *Atombau und Spektrallinien* (F. Vieweg & Sohn, Braunschweig, 1931).
- ⁷N. W. Ashcroft and N. D. Mermin, *Solid State Physics* (Saunders College Publishing, Ford Worth, 1976).
- ⁸R. Redmer, *Phys. Rep.* **282**, 35 (1997).
- ⁹K. Ishikawa, B. Felderhof, T. Blenski, and B. Cichocki, *J. Plasma Phys.* **60**, 787 (1998).
- ¹⁰L. J. Spitzer, *The physics of fully ionized plasmas* (Wiley Interscience, New York, 1962).
- ¹¹H. A. Kramers, *London, Edinburgh, and Dublin Philosophical Magazine and Journal of Science* **49**, 836 (1923).
- ¹²J. A. Gaunt, *Phil. Trans. R. Soc. London* **A229**, 163 (1930).
- ¹³W. J. Karzas and R. Latter, *Astrophys. J. Suppl.* **6**, 167 (1961).
- ¹⁴R. S. Sutherland, *Mon. Not. R. Astron. Soc.* **300**, 321 (1998).
- ¹⁵P. A. M. van Hoof, R. J. R. Williams, K. Volk, M. Chatzikos, G. J. Ferland, M. Lykins, R. L. Porter, and Y. Wang, *Mon. Not. R. Astron. Soc.* **444**, 420 (2014).
- ¹⁶M. de Avillez and D. Breitschwerdt, *Astron. Astrophys.* **580**, A124 (2015).
- ¹⁷F. Reif, *Fundamentals of statistical and thermal physics* (Waveland Press Inc., Long Grove, Illinois, 2009).
- ¹⁸A. Einstein, *Deutsche Physikalische Gesellschaft* **18**, 318 (1916).
- ¹⁹M. Abramowitz (editor) and I. A. Stegun (editor), *Handbook of mathematical functions with formulas, graphs, and mathematical tables* (U. S. Government Printing Office, Washington, D. C, 1964).
- ²⁰F. W. J. Olver (editor), D. W. Lozier (editor), R. F. Boisvert (editor), and C. W. Clark (editor), *NIST Handbook of Mathematical Functions* (Cambridge University Press and National Institute of Standards and Technology, 2010).
- ²¹V. Berestetskii, E. Lifshitz, and L. P. Pitaevski, *Relativistic Quantum Theory*, Course in Theoretical Physics, Vol. 4 (Pergamon Press, Oxford, 1971).
- ²²V. P. Krainov, *J. Phys. B: At. Mol. Opt. Phys.* **33**, 1585 (2000).
- ²³V. P. Krainov, *J. Exp. Theor. Physics* **92**, 960 (2001).
- ²⁴S. Chandrasekhar, *An Introduction to the Study of Stellar Structure* (Dover Publications Inc., New York, 1967).
- ²⁵J. Christensen-Dalsgaard, W. Däppen, S. V. Ajukov, E. R. Anderson, H. M. Antia, S. Basu, V. A. Baturin, G. Berthomieu, B. Chaboyer, S. M. Chitre, A. N. Cox, P. Demarque, J. Donatowicz, W. A. Dziembowski, M. Gabriel, D. O. Gough, D. B. Guenther, J. A. Guzik, J. W. Harvey, F. Hill, G. Houdek, C. A. Iglesias, A. G. Kosovichev, J. W. Leibacher, P. Morel, C. R. Proffitt, J. Provost, J. Reiter, E. J. Rhodes Jr., F. J. Rogers, I. W. Roxburgh, M. J. Thompson, and R. K. Ulrich, *Science* **272**, 1286 (1996).
- ²⁶S. Ichimaru, *Statistical Plasma Physics*, Vol. II: Condensed Plasmas (Addison Wesley, Reading, MA, 1994).
- ²⁷J. Wesson, *Tokamaks* (Clarendon Press, Oxford, 1987) p. 40.
- ²⁸One may conjecture that this limit corresponds to the limit $\omega \rightarrow 0$, had we treated Debye screening correctly, and one is tempted to substitute $\sqrt{\omega^2 + \omega_p^2}$ for ω under the logarithm in Eq. 47.
- ²⁹J. Pearson, *Computation of Hypergeometric Functions*, Ph.D. thesis, University of Oxford (2009).
- ³⁰P. J. Brussaard and H. C. van de Hulst, *Rev. Mod. Physics* **34**, 507 (1962).
- ³¹W. H. Press, S. A. Teukolsky, W. T. Vetterling, and B. P. Flannery, *Numerical Recipes in C* (Cambridge University Press, Cambridge, 1992).
- ³²I. P. Shkarofsky, T. W. Johnston, and M. P. Bachynski, *The particle kinetics of plasmas* (Addison-Wesley, Reading, Massachusetts, 1966).